

Measured turbulent mixing in a small-scale circuit breaker model

N. P. T. Basse,* R. Bini, and M. Seeger

ABB Switzerland Ltd., Corporate Research, Baden-Dättwil, CH-5405, Switzerland

*Corresponding author: nils.basse@ch.abb.com

Received 29 June 2009; revised 17 September 2009; accepted 16 October 2009;
posted 26 October 2009 (Doc. ID 113552); published 9 November 2009

The performance of high voltage gas circuit breakers depends on the temperature distribution of hot gas or plasma from the arc zone mixed with cold gas that is present, for example, in the exhausts and mixing volume. Understanding the details of the mixing process is imperative to estimate the temperature distribution within the entire breaker volume. Design studies rely on computational fluid dynamics (CFD) simulations to search for the best way to achieve satisfactory mixing. One key uncertainty in the CFD simulations is the role of turbulence in this process and how to properly account for it. To gain knowledge of the mixing process between hot and cold gases, we have constructed a simplified breaker geometry that is flexible and accessible to diagnostics. Apart from standard measurements of current and arc voltage, we measure pressure in the arc zone and the mixing volume. Further, the mixing volume is specially designed to be transparent, allowing us to make shadowgraphy measurements of the turbulent mixing during and after the arcing phase. We report on experiments performed in air at atmospheric pressure. © 2009 Optical Society of America

OCIS codes: 110.0115, 110.2960.

1. Introduction

In high voltage (HV) gas circuit breakers [1,2], short-circuit currents are interrupted by extinguishing arcs in a gaseous medium. This arc interruption process is quite complex and involves, e.g., flow effects to stabilize the arc on-axis and cool the arc by shear flow generated turbulence.

Both of these effects depend on gas flowing from the mixing volume, which is the volume where pressure is built up using the arc energy during the discharge. Therefore it is important to understand how hot gas from the arc zone mixes with colder gas in the mixing volume. This mixing process determines not only the blowing pressure but also the “quality” of the blowing gas, which is important for successful dielectric interruption in the post-arc phase [3–6]. By quality of the blowing gas, we mean for example the homogeneity, temperature, and density. To conform

with our standard nomenclature, we will denote the mixing volume as the heating volume in the remainder of this paper.

Arc physics and flow phenomena in HV gas circuit breakers are usually studied with the aid of computational fluid dynamics (CFD) simulations [7,8]. In particular, how to properly account for turbulent effects and their importance remains a major source of uncertainty. For example, it is known that turbulence does not play an important role in determining integral quantities such as pressure build up in the heating volume, for which laminar models are successfully applied [9]. However, when analyzing the local distribution of flow quantities such as temperature, the energy and momentum transfer can be significantly affected by turbulent structures.

To make progress towards an understanding of the actual behavior of turbulent mixing in the heating volume, we constructed a simple small-scale model of a gas circuit breaker. The heating volume was a two-dimensional (2D) slab with walls made of polymethyl methacrylate (PMMA), allowing us to

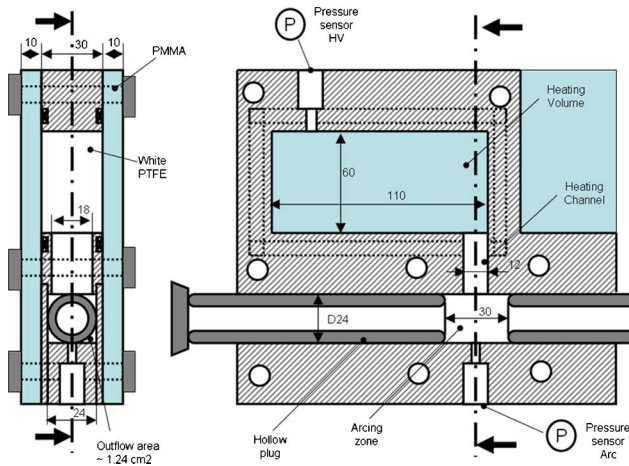


Fig. 1. (Color online) Design drawing of the small-scale model.

measure refractive index variations therein using “focused” shadowgraphy [10]. The images enable, e.g., a qualitative understanding of the flow phenomena and extraction of the velocity field. Local measurements of pressure and temperature in the heating volume have previously been performed [11]. Imaging of the flow in part of a three-dimensional (3D) heating volume has also been carried out [12]. However, to the best of our knowledge, imaging of turbulence in the entire heating volume as presented herein has not been published before.

In contrast to turbulence in the heating volume, turbulence in the arc zone has been extensively measured, especially in the 1970s. The diagnostic techniques used were schlieren imaging [13], pulsed holography [14], and differential interferometry [15,16].

This paper is organized as follows: In Section 2 we introduce the small-scale circuit breaker test device along with the various diagnostics used. The main results are collected in Section 3, and future work is outlined in Section 4. Finally, conclusions are drawn in Section 5.

2. Experimental Setup

A. Small-Scale Circuit Breaker Model

The layout of the small-scale circuit breaker model is shown in Fig. 1. The device is mounted in an open gas insulated switchgear tank: The arc burns in air at ambient pressure. It consists of two main parts made of white polytetrafluoroethylene (PTFE), which are mounted above and below the hollow plugs and clamped together with two PMMA sheets, each 10 mm thick. Thin PTFE sheets are placed laterally between the plugs and the PMMA to enclose the arc by ablating material. The assembly is held together with eight screws. From the arc zone between the hollow plugs a straight heating channel (HC) leads the ablated vapor to the rectangular heating volume. The length of the HC is 30 mm with an area of approximately 1.85 cm². The total outflow area along the outside of the plugs is about 2.5 cm², thus the minimum flow area is in the HC throat. The heating volume is 30 mm deep; it is assumed that this is sufficiently thin to limit the observed behavior to being 2D.

B. Diagnostics

1. Current and Voltage

The current and arc voltage of the discharge analyzed are collected in Fig. 2. The current is measured with a 1 : 10 differential voltage probe across a resistive shunt (40 μΩ). The arc voltage is measured using a capacitive-resistive voltage divider. The LC circuit ($L = 500 \mu\text{H}$, $C = 20 \text{ mF}$) generated AC current with a frequency of 50 Hz. The charging voltage was 1.75 kV.

We applied current for one half-wave. The peak current was just below 10 kA; combined with the 100 V arc voltage, this yields a peak power of 1 MW. The time axis is shifted so that current zero (CZ) is at 0.0 s; this is the case for all plots in this paper including time-varying quantities. The spikes in

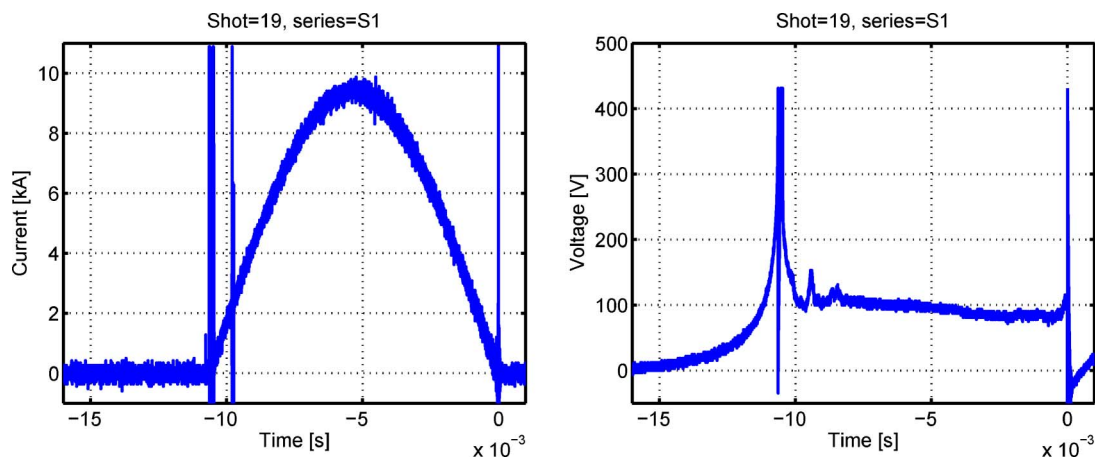


Fig. 2. (Color online) Left: current; right, arc voltage.

the current measurement are due to disturbances caused by the arc voltage.

Before current flows, the voltage across the contacts increases until a breakdown occurs (-11 ms). This is due to the contact resistance between the wire and the arcing contacts. Thereafter the Cu ignition wire heats up due to the current flowing through it and finally evaporates.

2. Pressure

Pressure is measured both in the arc zone and in the heating volume; see Fig. 1. Both sensors are piezoresistive and protected from the hot gas by a combination of PTFE tubes and metal adapters.

3. Turbulence Using Shadowgraphy

The main purpose of the work described in this paper is to measure turbulent mixing in the heating volume. To this end we found that the “focused” shadowgraphy [10] method was well suited.

Three components are required for shadowgraphy measurements: a light source, the object to be investigated (in our case a gas cloud), and a screen. Light from the source passes through the object and is refracted an angle ϵ . It can be shown using geometrical optics considerations that the refraction angle is proportional to the spatial derivative of the index of refraction perpendicular to the incident light rays. The derivation can be found in, e.g., Appendix A.6 of [10].

The term “focused” shadowgraphy is used in [10] and is taken to describe a setup where (i) the light from the source is collimated before passing through the object and (ii) the shadowgram is condensed or expanded after the object. In the remainder of the paper, we will simply denote the technique shadowgraphy.

The contrast of a shadowgram, i.e., the ratio of the change of illuminance because of the object to the undisturbed illuminance, has been shown to be proportional to the refraction angle divided by the perpendicular dimension of the object [17]. For a small object, this quantity is equal to the spatial derivative of the refraction angle, i.e., the Laplacian of the index of refraction [18].

4. Shadowgraphy Setup

A principle sketch of the optical setup is shown in Fig. 3. The setup consists of four parts: transmitting optics, test object, receiving optics, and a complementary metal oxide semiconductor high speed camera. The transmitting optics begins with a light source, in our case a 20 mW He–Ne laser that has a wavelength of 632.8 nm. The laser beam is expanded by a microscope objective ($20\times$ magnification), and the expanded beam is made parallel (collimated) by a lens having a focal length of 1000 mm. The lens diameter is 140 mm, i.e., $f/7.1$. The beam diameter through the test object is roughly 120 mm.

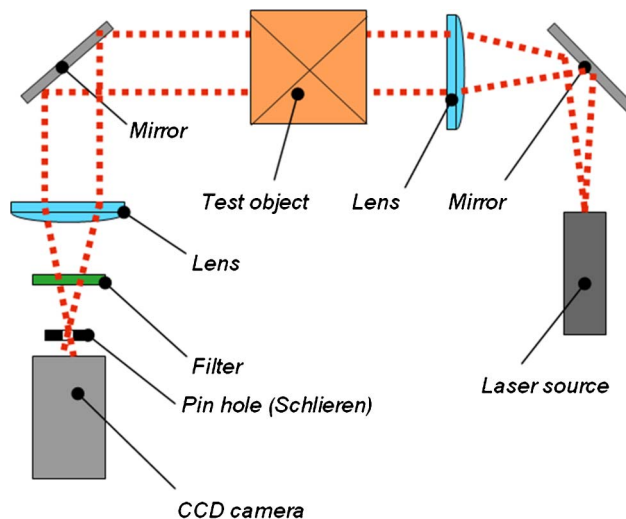


Fig. 3. (Color online) Sketch of the shadowgraphy setup.

The receiving optics assembly is composed of a lens having a focal length of 830 mm followed by a gray filter (letting 10.2% of the light through) to reduce the beam power. A narrow He–Ne filter after the gray filter makes sure that only light at the He–Ne wavelength is detected, and a 2 mm diameter pinhole at the back focal plane of the 830 mm lens stops scattered arc zone light from entering the complementary metal oxide semiconductor camera [19]. A 50 mm objective is mounted on the camera. We sample the camera at 32,000 frames per second ($31.25\ \mu\text{s}$ between frames) with an exposure time of $1\ \mu\text{s}$. The area used on the chip is 320 (width) \times 240 (height) pixels.

3. Results

A. Pressure

The measured pressures are shown in Fig. 4. Strong transients occur early in the discharge until about

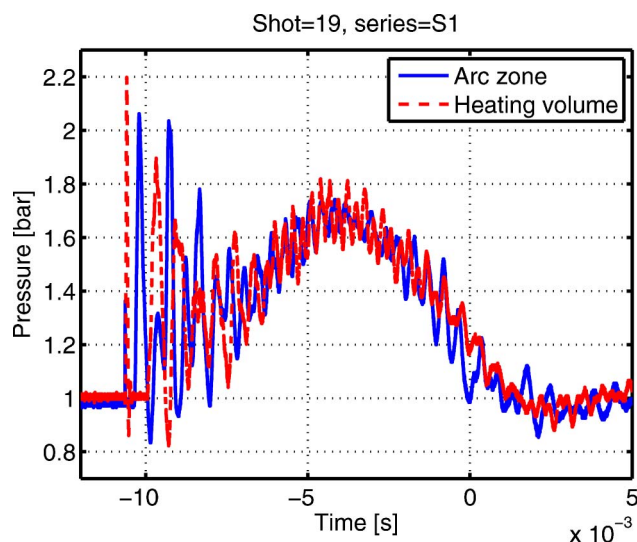


Fig. 4. (Color online) Arc zone pressure (solid line) and heating volume pressure (dashed line).

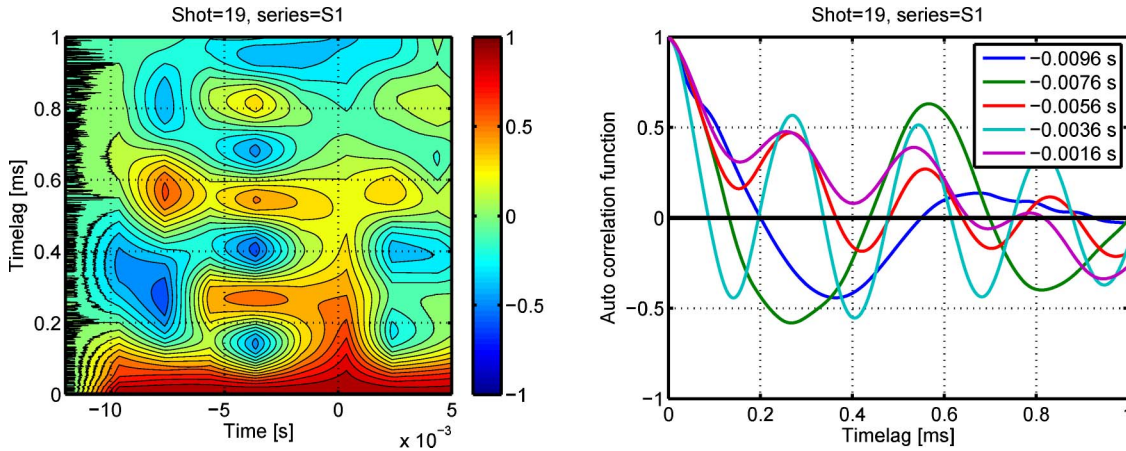


Fig. 5. (Color online) Autocorrelation of the heating volume pressure. Left, contour plot; right, 2D plot.

–7 ms, thereafter the oscillations settle down with a lower amplitude. The peak pressure reaches 1.6–1.7 bars at peak current, a 60%–70% increase, both in the arc zone and in the heating volume.

Using circuit breaker terminology, backheating takes place during the high current phase. Thereafter the arc shrinks, leading to a flow reversal from the heating volume to the arc zone. Around CZ the heating volume pressure is slightly higher than the arc zone pressure.

1. Arc Pressure

We have observed clear signs of oscillations in both the arc zone and heating volume pressure; see Fig. 4. These oscillations are pressure waves propagating through the test device at the speed of sound.

To quantify the oscillation period of the arc pressure, we calculate the autocorrelation [20] of the arc zone pressure signal. Throughout the discharge a correlation is observed at a time lag of 0.2 ms, corresponding to a period of 0.4 ms or a frequency of 2.5 kHz.

2. Heating Volume Pressure

As for the arc zone pressure, we also calculate the autocorrelation function for the heating volume pressure; see Fig. 5. From the contour plot we observe that the characteristic pressure oscillation frequency changes from the backheating to the outflow phase. The time lag in the first phase is about 0.3 ms (frequency 1.5 kHz), in the last phase roughly 0.15 ms (3 kHz). These time lags are the minima closest to

zero time lag. See also Table 1 for the exact frequency versus time at five instances during the discharge.

The oscillations are pressure waves being reflected from the walls of the heating volume. The three fundamental speeds are

$$\begin{aligned} v_x &= f \times 2 \times L_x, & v_y &= f \times 2 \times L_y, \\ v_z &= f \times 2 \times L_z, \end{aligned} \quad (1)$$

where f is the frequency, $L_x = 110$ mm, $L_y = 60$ mm, and $L_z = 30$ mm. These speeds can be calculated based on the frequencies found from the autocorrelation function; see Table 1. Further, the temperature corresponding to those speeds can be extracted with the help of the sound speed of air as a function of temperature; see Fig. 6. The curve begins at 300 K, where the sound speed is 340 m/s; note that this curve is independent of pressures in the range we observe (1–2 bars). Temperature is not written in Table 1, where it is estimated to be below room temperature, i.e., 300 K.

To determine which speed is the one to be used, we make two additional tests:

1. We calculate the fast Fourier transform (FFT) of the heating volume pressure; see Fig. 7. The contour plot shows two co-existing features, one at 1.5 kHz and one at 3.5 kHz. The 1.5 kHz feature dominates in the first half of the discharge and the 3.5 kHz feature is largest in the second half of the discharge. This means that the wave traveling along the x axis dominates in the beginning and the wave traveling along the y axis is most prominent during

Table 1. Overview of Resonance Speeds^a

Time (s)	f (kHz)	v_x (m/s)	T_x (K)	v_y (m/s)	T_y (K)	v_z (m/s)	T_z (K)
–0.0096	1.4	308	-	168	-	84	-
–0.0076	1.9	418	439	228	-	114	-
–0.0056	3.3	726	1396	396	391	198	-
–0.0036	3.6	792	1683	432	471	216	-
–0.0016	3.3	726	1396	396	391	198	-

^aThe predicted temperature is written in bold.

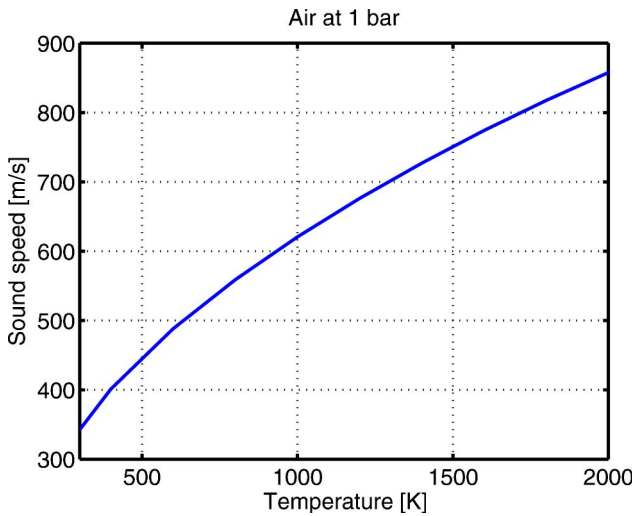


Fig. 6. (Color online) Sound speed of air at 1 bar as a function of temperature.

the final phase of the discharge. The transition occurs between -7.6 and -5.6 ms. The maximum temperature is reached at -3.6 ms and is 471 K; see Table 1.

2. We estimate the upper limit of the temperature increase. If we assume that the density stays constant in the heating volume, the temperature increase is proportional to the pressure increase. Since the peak pressure increase is about 65%, the temperature increase can at most also be a 65% increase from 300 K, which is 495 K. If the density increases in the heating volume as well during the backheating phase, the temperature increase will be smaller than this value. This implies that the temperature calculated from the x -axis speeds is too high from -5.6 ms onwards.

To conclude, we have arrived at the following understanding: During backheating, the pressure waves travel in the x -axis direction and in the out-flow phase, the pressure waves travel in the y -axis direction. The predicted temperature at different times is written in bold in Table 1.

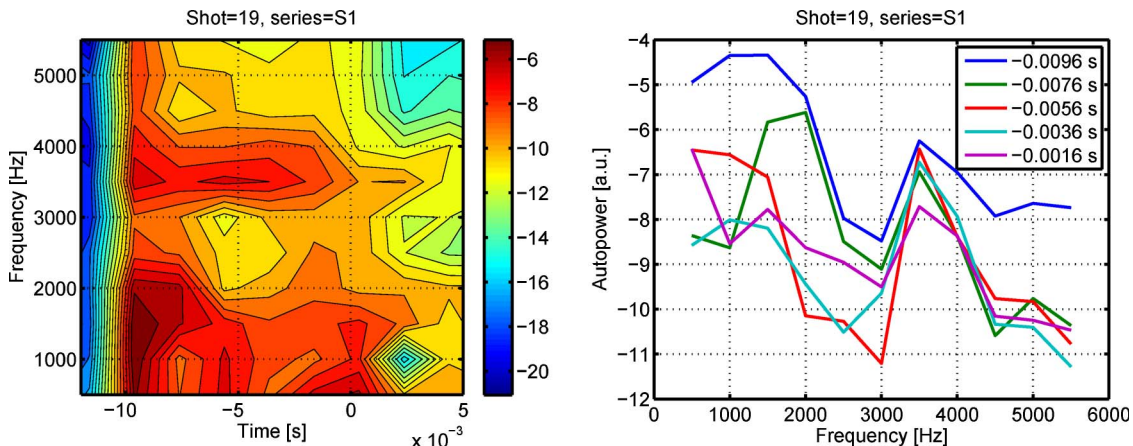


Fig. 7. (Color online) FFT of the heating volume pressure. Left, contour plot; right, 2D plot.

3. Relationship Between the Arc and Heating Volume Pressure

After the separate treatment of the arc zone pressure and heating volume pressure, we now turn to the interplay between them. The cross correlation is shown in Fig. 8. Two basic features in different phases can be discerned: first, from -10 to -6 ms, an oscillatory correlation with a peak at a time lag of -0.5 ms is found. This means that oscillations in both pressures are correlated and that the arc zone pressure changes 0.5 ms before the heating volume pressure. Second, from -6 to CZ a positive correlation is observed roughly at a time lag of 0.0 ms. This means the pressures are correlated—and in phase—during this period. The transition between the two features is most likely linked to the time of flow reversal, where flow is directed from the heating volume towards the arc zone.

B. Turbulence

For the reader to get an impression of how the turbulent mixing develops, we have collected a small cartoon of shadowgraphy images in Fig. 9. The top left image (-12 ms) is the background image before the discharge. The heating channel is in the lower left-hand corner for all images.

At -10 ms, early in the discharge, two features can be seen: the first is shock waves propagating through the heating volume and bouncing off the walls at different angles. The second is a turbulent cloud emanating from the heating channel. The turbulent cloud expands upwards at a speed of about 40 m/s early on, i.e., around -10 ms.

At -8 ms the shock waves have subsided but the turbulent cloud continues to expand. It is now expanding sideways at a speed of roughly 15 m/s.

From the turbulent cloud, a large vortex rotating in the clockwise direction develops. This vortex is visible from -6 ms onward. The vortex expands through the heating volume until it fills the entire heating volume. This happens in the vicinity of CZ.

Flow reversal occurs about 4 ms before CZ (at peak pressure; see Fig. 4). Gas from the heating volume

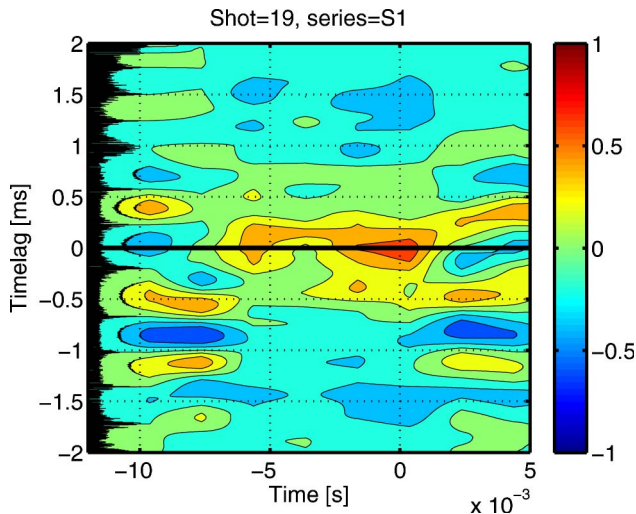


Fig. 8. (Color online) Cross correlation function between the arc zone and heating volume pressures.

begins to flow back into the arc zone. The estimated speed of this gas at the HC entrance/exit is 30 m/s. Note: the bright patch at the bottom left of the images at -6 and -4 ms is due to light emitted by the arc. This light is particularly strong close to the peak current phase.

1. Velocimetry

Velocimetry of flow measurements has been done by various authors in the past, for example using image correlation velocimetry on flows with markers (particle seeding) [21–23] or velocimetry of schlieren images without markers [24,25]. While the above mentioned methods yield quite good results, our aim was to apply a straightforward cross correlation technique where we assume that the turbulent structures do not deform between frames. Work of this type can be found, e.g., in [26], where it is called schlieren “particle image velocimetry”. An improved version of this technique was published in [27]. We use the approach from [26] but with shadowgraphy instead of schlieren, i.e. shadowgraphy “particle image velocimetry”. We use shadowgraphy because this method gave the highest quality images.

Traditionally, flows have been measured by seeding the flow with markers that are easily tracked. Over the last few decades, the structures in the flows have themselves been used as markers, eliminating the need to seed the flow. We assume that the flow observed is 2D.

The basic procedure makes use of the 2D cross correlation function between two sequential frames. The main routine to perform the correlations has been taken from [28]. We will describe an example in the following to illustrate this method.

First one begins with two images; we use those in Fig. 10. By visual inspection these images are nearly impossible to distinguish. The purpose of the post-processing described is to extract the velocity field from these two frames. One does this by calculating

the cross correlation function between subwindows of the full images. We use 64×64 pixels as our window size. The window in one image is kept fixed, while the window in the other image is moved around to cover the entire image. The step size of these movements has been chosen to 8 pixels. Once this is complete, the fixed image is moved and the whole procedure is repeated. This process continues until the fixed image windows have covered the entire image.

For our shadowgraphy setup, 1 pixel corresponds to 0.36 mm, so 8 (64) pixels is a distance of 2.9 (23.0) mm, respectively. The maximum detectable speed for purely vertical or horizontal motion is 800 m/s.

For each calculated cross correlation, the peak is found that then tells us how many pixels a detected structure has moved from one frame to the next (if any). We also apply subsample interpolation to increase the accuracy of the result. For a certain percentage of the cross correlations the procedure will fail, i.e., the peak of the cross correlation function is at the border of the subwindow. We denote these cases nonconvergent correlations.

To avoid problems related to the implementation of the normalized cross correlation function in the programming language we use, we have to add a border of zeros around one of the images being correlated. The optimum amount of border pixels was found empirically by optimizing the percentage of converged correlations of the subwindows; see Fig. 11. The ideal size of the border was found to be 2 pixels. This evaluation is shown for a time after flow reversal, but the result is independent of the time chosen for the border analysis.

It is instructive to plot the percentage of converged correlations as a function of time for the chosen 2 pixel border; see Fig. 12. Before the discharge begins, almost 100% of the correlations converge, i.e., the background noise has a maximum correlation at zero displacement. This value drops to about 20% in the phase where shock waves dominate the heating volume, since our cross correlation method is not able to track them. Following the shock wave phase, during backheating, the percentage is stable at about 50% until after flow reversal, where the percentage increases monotonically as the vortex fills up the heating volume. Structures in the vortex are successfully tracked during this vortex expansion phase. The increase persists until a few ms after CZ, where the percentage is almost back to 100%.

The main result of our analysis is the velocity field, an example of which is shown in Fig. 13. The time shown is 2.5 ms before CZ where the vortex rotating clockwise is clearly visible, indicating the feasibility of the cross correlation procedure. The length of the arrows indicates the speed of the dominating turbulent structure in the given subwindow. The maximum velocity is found at the left-hand side of the vortex center. The modest velocity at the right-hand side of the vortex center may be due to a lack of laser light in this region of the heating volume.

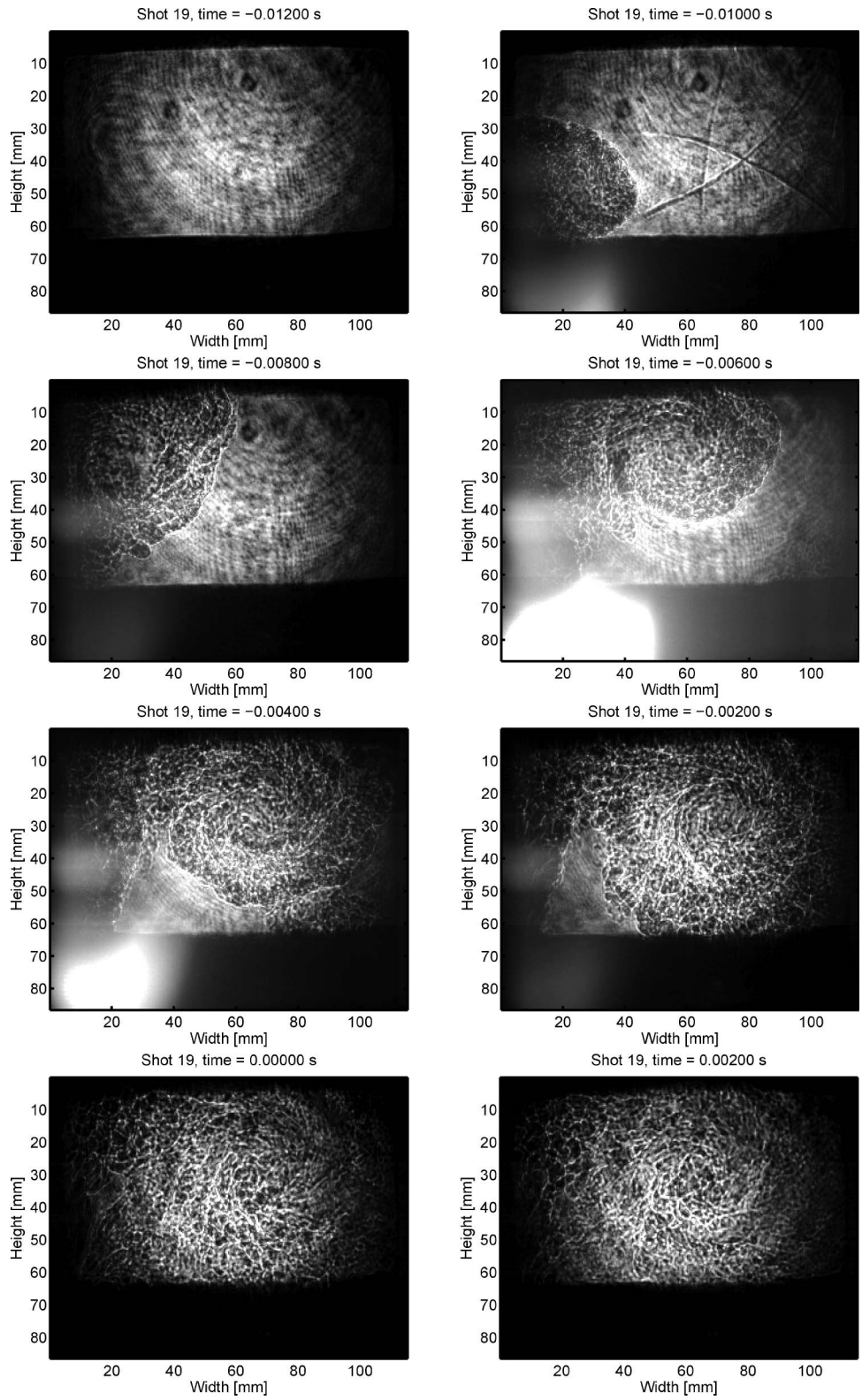


Fig. 9. Cartoon of the mixing process as measured using shadowgraphy (Media 1).

The velocity field in Fig. 13 contains information regarding the velocity of individual structures in the vortex; it is not directly related to the expansion velocity of the vortex inside the heating volume.

The absolute speed can be derived from the velocity field if the sample rate and the length of one pixel are known. Converting the velocity field to the speed field, one arrives at a plot such as the

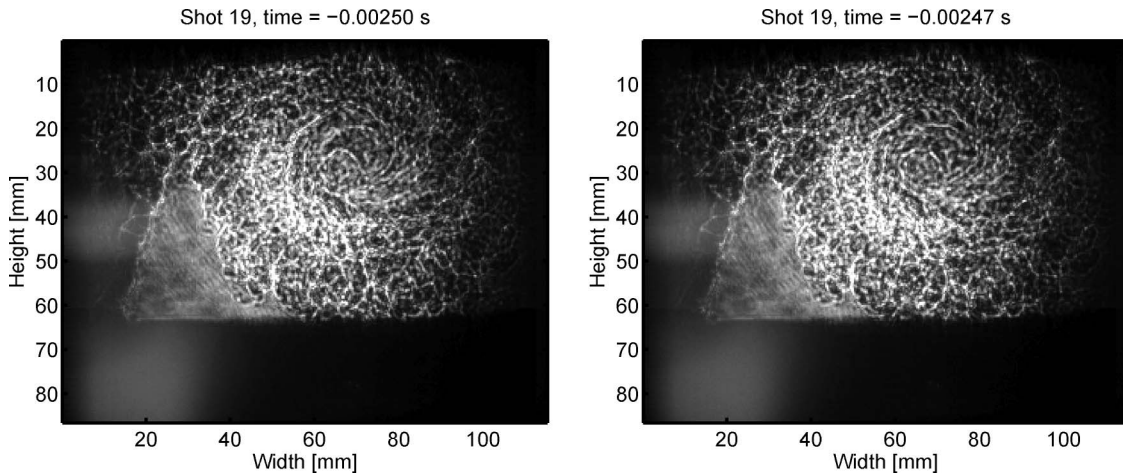


Fig. 10. Two sequential shadowgraphy images.

one in Fig. 14. The typical speed is 10–20 m/s. The velocity and speed fields are useful for comparisons to the output of CFD simulations. This will be demonstrated in a subsequent paper.

One can use the speed field for further processing, for example to evaluate the mean and standard deviation of the speed in the entire heating volume versus time. These quantities are shown in Fig. 15 along with the relative uncertainty of the speed. The mean speed rises to 10 m/s during the early backheating phase, subsequently drops slightly, and then increases to 10 m/s again around flow reversal. Towards CZ the mean speed then decreases somewhat. The standard deviation stays at 5 m/s during the entire discharge. So the typical speed of turbulent structures in the vortex is 10 ± 5 m/s. The relative uncertainty is 1 (100%) during the initial backheating and then reduces to 0.5 (50%) for the remainder of the shot.

One also has the option to monitor the speed and velocity components at a fixed point. We show this

information for a point at the bottom center of the heating volume in Fig. 16. No systematic behavior is observed previous to 5 ms before CZ, where the X component (horizontal) suddenly appears at -15 m/s; the negative sign indicates that the flow is directed towards the in-outlet. The Y component (vertical) is close to zero. The horizontal velocity component decreases in magnitude until 2 ms before CZ, whereafter it then accelerates again until a few ms after CZ.

4. Outlook

There are several open points to pursue that can be divided into three categories: improvements of diagnostics and the experimental setup, refined measurement analysis tools, and CFD simulations. These points are discussed below.

A. Experiments

Several optical techniques have been compared to evaluate their suitability for our particular situation.

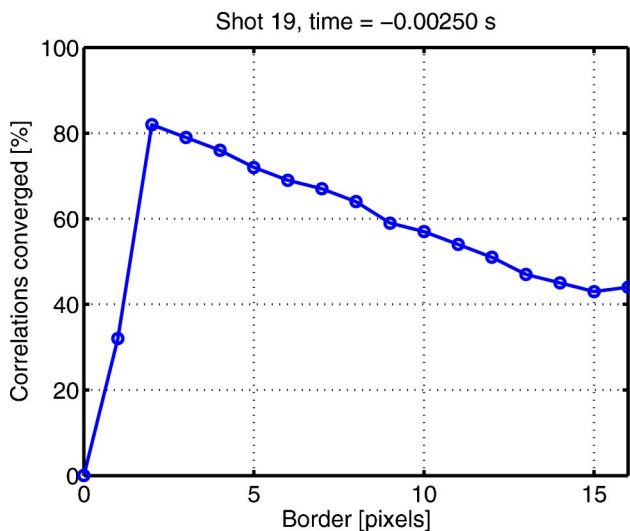


Fig. 11. (Color online) Percentage of converged correlations versus the number of border pixels.

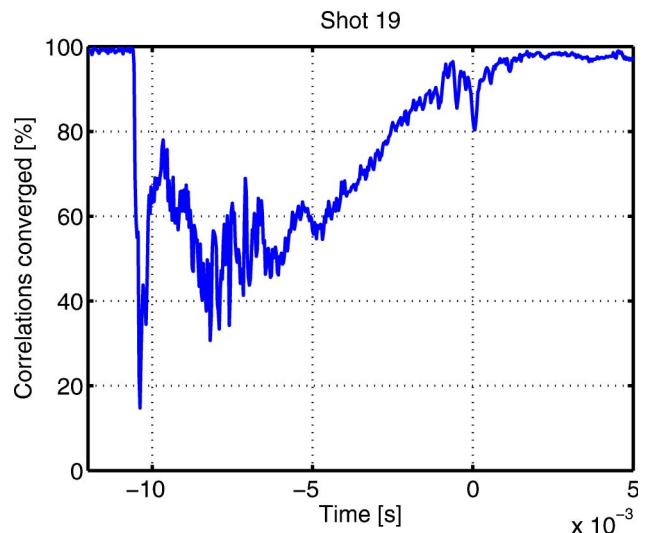


Fig. 12. (Color online) Percentage of converged correlations as a function of time for the 2 pixel border.

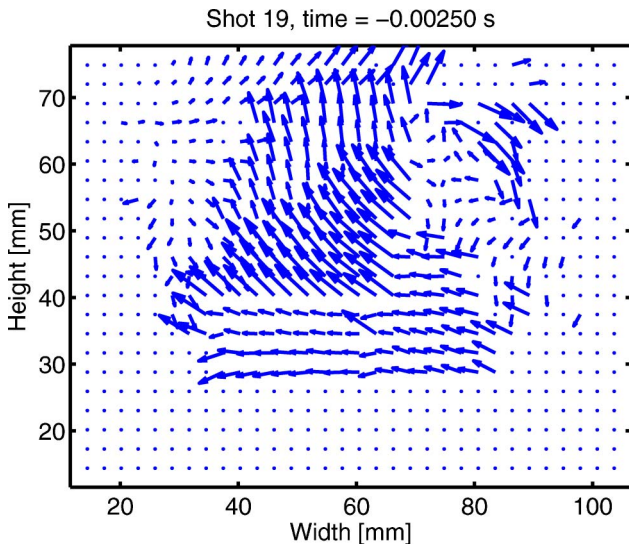


Fig. 13. (Color online) Heating volume velocity field 2.5 ms before CZ.

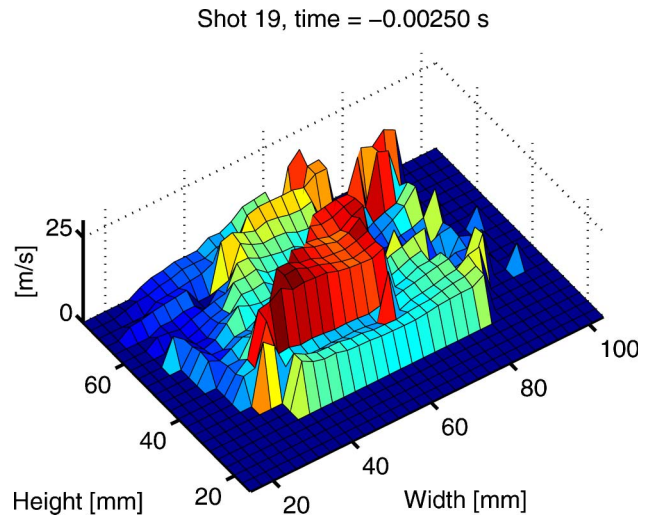


Fig. 14. (Color online) Heating volume speed field 2.5 ms before CZ.

This comparative study will be published elsewhere. A fast temperature measurement with a time resolution of the order of 1 ms would be very useful for calibration of our mean temperature estimates. This could perhaps be done using the measured breakdown voltage across microgaps in the heating volume [11].

Igniting the arc using moveable arcing contacts instead of an ignition wire would be desirable to avoid the pressure peak associated with the wire explosion. This would also allow us to establish whether the early shock waves occur only because of the ignition wire or if they are inherent to the process.

Having such a flexible test device as the one introduced herein opens up a wide range of topics for investigation. For example, the influence of different fill pressures or gases on the mixing behavior. Another appealing topic is to elucidate how a different shape of the heating volume affects the mixing pro-

cess. Such an investigation would have direct relevance for circuit breaker design.

B. Analysis of Measurements

Several analysis methods remain to be applied to our data, including more advanced velocimetry analysis enabling shock wave tracking, 2D spatial FFTs to study the power-law decay of turbulent structures as a function of the spatial scale [29–33], extraction of the density field from mass conservation [34], and autocorrelation analysis to determine the lifetime of turbulent structures [35–38]. It might also be possible to infer the temperature field from the velocity field [39]. These techniques are outside the scope of this paper and will be left for future studies.

C. Computational Fluid Dynamics Simulations

One of the main reasons to perform the experiments described in this paper is to compare the measurements to CFD simulations. This comparison has not been included in the present paper but has been

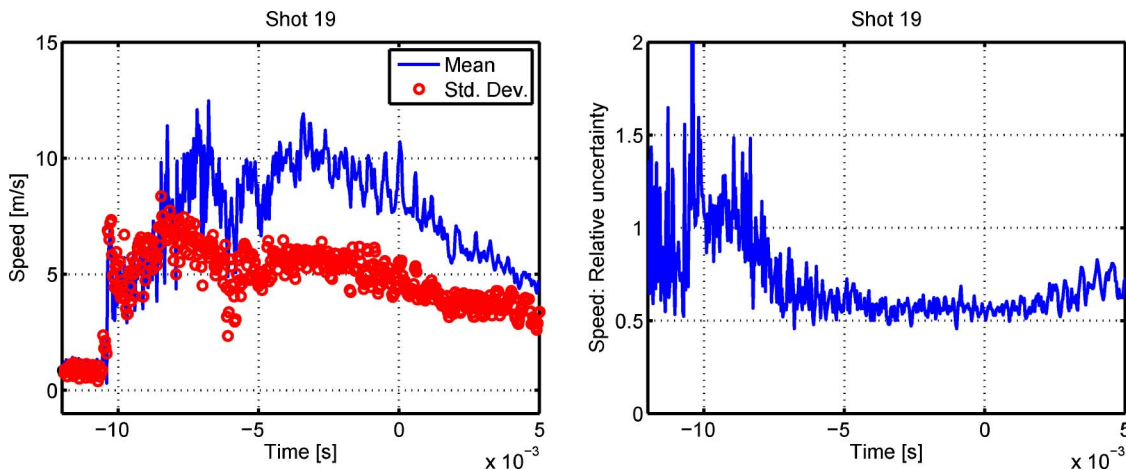


Fig. 15. (Color online) Left, mean (solid line) and standard deviation (open circles) of speed in the heating volume versus time. Right, relative uncertainty of speed versus time.

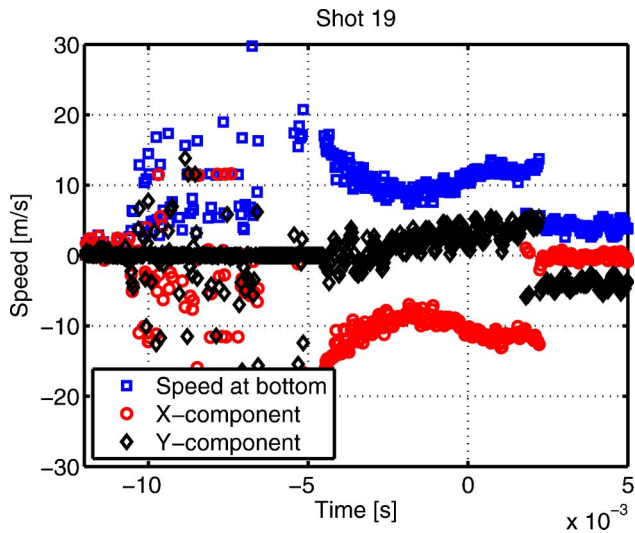


Fig. 16. (Color online) Speed at the bottom center of the heating volume versus time: speed (open squares), X component (open circles) and Y component (open diamonds).

completed and will be published elsewhere. To provide the reader with some sense of the outcome of this comparative study, we have collected the main points discovered so far:

- To obtain a velocity field in reasonable agreement with the measurements, it is necessary to include a turbulence model in the CFD simulations.
- The similarity between 2D and 3D CFD simulations showed that the mixing behavior is 2D, i.e., the depth of the heating volume is sufficiently thin.

5. Conclusions

In this paper we have introduced a versatile, two-dimensional, small-scale circuit breaker model. It has been built to study turbulence in the heating volume, using shadowgraphy as the primary diagnostic. Additionally, pressure was measured in both the arc zone and the heating volume.

In the discharge analyzed, the current consisted of one half-wave at 50 Hz with a peak current of just below 10 kA. The arc was burning in air at atmospheric pressure.

Shock waves were observed during the initial backheating phase with shadowgraphy. Average speeds of pressure oscillations in the model breaker were derived using autocorrelation functions of the pressure measurements. From this analysis we estimated the average temperature in the heating volume and discovered that the shock waves travel horizontally during backheating and vertically in the outflow phase.

The formation and expansion of a turbulent cloud from the heating volume inlet/outlet was measured using shadowgraphy and the velocity field of the vortex developing from the turbulent cloud was extracted. The speed of turbulence in the vortex was in the range 10–20 m/s. Complete mixing was established before CZ. Our findings will be quantitatively compared to CFD simulations in future publications.

We thank Felix Rager and Jens Knauel for valuable assistance in preparation and execution of the experiments treated in this paper. We are grateful to Benjamin Wüthrich for supplying the basic velocity cross correlation routine.

References

1. T. Jakob, E. Schade, and R. Schaumann, "Self-blasting, a new switching principle for economical SF₆ circuit breakers," *Proceedings of the IEE Conference CIREN* (Institution of Electrical Engineers, 1977), pp. 63–66.
2. C. M. Franck and M. Seeger, "Application of high current and current zero simulations of high-voltage circuit breakers," *Contrib. Plasma Physics* **46**, 787–797 (2006).
3. E. Schade and K. Ragaller, "Dielectric recovery of an axially blown SF₆-arc after current zero: Part I—Experimental investigations," *IEEE Trans. Plasma Science* **PS-10**, 141–153 (1982).
4. K. Ragaller, W. Egli, and K. P. Brand, "Dielectric recovery of an axially blown SF₆-arc after current zero: Part II—Theoretical investigations," *IEEE Trans. Plasma Science* **PS-10**, 154–162 (1982).
5. K. P. Brand, W. Egli, L. Niemeyer, K. Ragaller, and E. Schade, "Dielectric recovery of an axially blown SF₆-arc after current zero: Part III—Comparison of experiment and theory," *IEEE Trans. Plasma Science* **PS-10**, 162–172 (1982).
6. H. M. Ryan, *High Voltage Engineering and Testing*, 2nd ed. (Institute of Engineering and Technology, 2001).
7. H. Nordborg and A. A. Iordanidis, "Self-consistent radiation based modelling of electric arcs: I. Efficient radiation approximations," *J. Phys. D: Appl. Phys.* **41**, 135205 (2008).
8. A. A. Iordanidis and C. M. Franck, "Self-consistent radiation-based simulation of electric arcs: II. Application to gas circuit breakers," *J. Phys. D: Appl. Phys.* **41**, 135206 (2008).
9. N. P. Basse, M. M. Abrahamsson, M. Seeger, and T. Votteler, "Quantitative analysis of gas circuit breaker physics through direct comparison of 3-D simulations to experiment," *IEEE Trans. Plasma Sci.* **36**, 2566–2571 (2008).
10. G. S. Settles, *Schlieren and Shadowgraph Techniques*, 1st ed. (Springer-Verlag, 2006).
11. T. Shinkai, M. Ooi, T. Uchii, H. Kawano, T. Nakamoto, and H. Ikeda, "Gas density and temperature in thermal volume for self-blast interrupting chambers," in *Proceedings of the IEEE/PES T&D Asia Pacific Conference* (IEEE, 2002), pp. 419–423.
12. R. A. Puffer, "Experimentelle Untersuchung der Heissgasströmung in einem SF₆-Selbstblusschaltermodell mittels Particle Image Velocimetry (PIV) zur Verifikation von Simulationsmodellen," Ph.D. thesis (RWTH Aachen, Germany, 2001).
13. U. Kogelschatz and W. R. Schneider, "Quantitative schlieren techniques applied to high current arc investigations," *Appl. Opt.* **11**, 1822–1832 (1972).
14. B. Ineichen, U. Kogelschatz, and R. Dändliker, "Schlieren diagnostics and interferometry of an arc discharge using pulsed holography," *Appl. Opt.* **12**, 2554–2556 (1973).
15. U. Kogelschatz, "Application of a simple differential interferometer to high current arc discharges," *Appl. Opt.* **13**, 1749–1752 (1974).
16. D. W. Branston and J. Mentel, "Beugungstheoretische Behandlung eines Differentialinterferometers für ausgedehnte Phasenobjekte," *Appl. Phys.* **11**, 241–246 (1976).
17. H. Schardin, "Das Toeplersche Schlierenverfahren," *VDI-Forschungsheft 367* (VDI Verlag, 1934).
18. H. Hannes, "Über die Eigenschaften des Schattenverfahrens," *Optik (Jena)* **13**, 34–48 (1956).
19. Phantom v7.3 from Vision Research, Inc., Commercial model name used for technical communication only.

20. J. S. Bendat and A. G. Piersol, *Random Data*, 3rd ed. (Wiley, 2000).
21. P. T. Tokumaru and P. E. Dimotakis, "Image correlation velocimetry," *Exp. Fluids* **19**, 1–15 (1995).
22. K. M. Smith and J. C. Dutton, "A procedure for turbulent structure convection velocity measurements using time-correlated images," *Exp. Fluids* **27**, 244–250 (1999).
23. M. D. Alaimo, D. Magatti, F. Ferri, and M. A. C. Potenza, "Heterodyne speckle velocimetry," *Appl. Phys. Lett.* **88**, 191101 (2006).
24. E. Arnaud, E. Mémin, R. Sosa, and G. Artana, "A fluid motion estimator for schlieren image velocimetry," *Lecture Notes Comput. Sci.* **3954**, 198–210 (2006).
25. R. Sosa, E. Arnaud, E. Mémin, and G. Artana, "Schlieren image velocimetry applied to EHD flows," in *Proceedings of the International Symposium on Electrohydrodynamics* (2006), pp. 1–4.
26. D. R. Jonassen, G. S. Settles, and M. D. Tronosky, "Schlieren 'PIV' for turbulent flows," *Opt. Lasers Eng.* **44**, 190–207 (2006).
27. J. A. Volpe and G. S. Settles, "Laser-induced gas breakdown as a light source for schlieren and shadowgraph particle image velocimetry," *Opt. Eng. Lett.* **45**, 080509 (2006).
28. T. Rösgen, "Quantitative flow visualization," ETH Zürich Lecture Notes, version 1.4.2, 2005.
29. S. Chen, R. E. Ecke, G. L. Eyink, M. Rivera, M. Wan, and Z. Xiao, "Physical mechanism of the two-dimensional inverse energy cascade," *Phys. Rev. Lett.* **96**, 084502 (2006).
30. S. Chen, R. E. Ecke, G. L. Eyink, X. Wang, and Z. Xiao, "Physical mechanism of the two-dimensional enstrophy cascade," *Phys. Rev. Lett.* **91**, 214501 (2003).
31. S. Chen, G. Doolen, J. R. Herring, R. H. Kraichnan, S. A. Orszag, and Z. S. She, "Far-dissipation range of turbulence," *Phys. Rev. Lett.* **70**, 3051–3054 (1993).
32. S. P. Trainoff and D. S. Cannell, "Physical optics treatment of the shadowgraph," *Phys. Fluids* **14**, 1340–1363 (2002).
33. F. Crocco, D. Brogioli, A. Vailati, M. Giglio, and D. S. Cannell, "Nondiffusive decay of gradient-driven fluctuations in a free-diffusion process," *Phys. Rev. E* **76**, 041112 (2007).
34. I. J. Jagoda and F. J. Weinberg, "Optical studies of plasma jets," *J. Phys. D: Appl. Phys.* **13**, 551–561 (1980).
35. S. Zoletnik, M. Anton, M. Endler, S. Fiedler, M. Hirsch, K. McCormick, J. Schweinzer, and the W7-AS Team, "Density fluctuation phenomena in the scrape-off layer and edge plasma of the Wendelstein 7-AS stellarator," *Phys. Plasmas* **6**, 4239–4247 (1999).
36. F. Crocco, D. Brogioli, A. Vailati, M. Giglio, and D. S. Cannell, "Use of dynamic schlieren interferometry to study fluctuations during free diffusion," *Appl. Opt.* **45**, 2166–2173 (2006).
37. D. Magatti, M. D. Alaimo, M. A. C. Potenza, and F. Ferri, "Dynamic heterodyne near field scattering," *Appl. Phys. Lett.* **92**, 241101 (2008).
38. D. Brogioli, F. Crocco, V. Cassina, D. Salerno, and F. Mantegazza, "Nano-particle characterization by using exposure time dependent spectrum and scattering in the near field methods: How to get fast dynamics with low-speed CCD camera," *Opt. Express* **16**, 20272–20282 (2008).
39. G. Papadopoulos, "Novel shadow image velocimetry technique for inferring temperature," *J. Thermophys. Heat Transfer* **14**, 593–603 (2000).